Biophysical Journal
Article

Biophysical Society

Bacteriophytochrome Photoisomerization Proceeds Homogeneously Despite Heterogeneity in Ground State

Cheng Wang,[1] Moira L. Flanagan,[2] Ryan D. McGillicuddy,[1] Haibin Zheng,[1] Alan Ruvim Ginzburg,[1] Xiaojing Yang,[3] Keith Moffat,[3] and Gregory S. Engel[1,*]

[1]Department of Chemistry, The James Franck Institute, Institute for Biophysical Dyanmics, [2]Graduate Program in Biophysical Science, The James Franck Institute, Institute for Biophysical Dynamics, and [3]Department of Biochemistry and Molecular Biology, and Institute for Biophysical Dynamics, The University of Chicago, Chicago, Illinois

ABSTRACT Phytochromes are red/far-red photoreceptors that are widely distributed in plants and prokaryotes. Ultrafast photoisomerization of a double bond in a biliverdin cofactor or other linear tetrapyrrole drives their photoactivity, but their photodynamics are only partially understood. Multiexponential dynamics were observed in previous ultrafast spectroscopic studies and were attributed to heterogeneous populations of the pigment-protein complex. In this work, two-dimensional photon echo spectroscopy was applied to study dynamics of the bacteriophytochromes RpBphP2 and PaBphP. Two-dimensional photon echo spectroscopy can simultaneously resolve inhomogeneity in ensembles and fast dynamics by correlating pump wavelength with the emitted signal wavelength. The distribution of absorption and emission energies within the same state indicates an ensemble of heterogeneous protein environments that are spectroscopically distinct. However, the lifetimes of the dynamics are uniform across the ensemble, suggesting a homogeneous model involving sequential intermediates for the initial photodynamics of isomerization.

INTRODUCTION

Phytochromes are red/far-red photoreceptors in plants, fungi, and prokaryotes that regulate a wide variety of physiological processes (1–3). For example, the homodimeric bacteriophytochrome denoted RpBphP2 (P2) regulates the expression of photosynthetic light-harvesting LH4 complexes in *Rhodopseudomonas palustris* (4). The photochemistry of P2 is mediated by a Z-to-E isomerization of the C_{15}=C_{16} double bond of its linear tetrapyrrole cofactor, biliverdin-IXα (BV) (5,6). Details of the isomerization are not fully understood. Bacteriophytochromes interconvert between two spectrally distinct states, the P_r state with a red absorption peak at ~700 nm and the P_{fr} state with a far-red absorption peak at ~750 nm (Fig. 1). In P2, the dark state is P_r. The first step in the light-dependent $P_r \rightarrow P_{fr}$ transformation takes place in tens to hundreds of picoseconds with the formation of a Lumi-R intermediate state (6). The subsequent Lumi-R $\rightarrow P_{fr}$ transformation involves rearrangement of the protein matrix that can take up to hundreds of milliseconds (7,8), which modifies the activity of a covalently attached kinase effector domain and initiates signaling to downstream components. Reverse photochemistry of $P_{fr} \rightarrow P_r$ in P2 and similar bacteriophytochromes can occur thermally or by absorption of a second photon of far-red light proceeding through a Lumi-F intermediate (9). Because the $P_r \rightarrow P_{fr}$ and $P_{fr} \rightarrow P_r$ reactions each require one photon and are completely separate, the $P_{fr} \rightarrow P_r$ reaction need not be the reverse of the $P_r \rightarrow P_{fr}$ reaction.

Reaction dynamics of the $P_r \rightarrow$ Lumi-R transformation have been examined by various spectroscopic methods, including pump-probe spectroscopies (10–15), femtosecond-stimulated Raman spectroscopy (16), and picosecond time-resolved fluorescence spectroscopy (5,17). Multiexponential decays were commonly observed (10–15,18), with component lifetimes spanning four orders of magnitude (0.1–0.7 ps, 2–6 ps, 20–70 ps, and 120–400 ps). In the literature, the multiple lifetimes have been explained by either a homogeneous model involving sequential intermediates or a heterogeneous model invoking functionally distinct pathways, but no conclusion has been reached (15,19). Here, we clarify this discrepancy by exploring bacteriophytochromes with

Submitted July 29, 2016, and accepted for publication October 11, 2016.

*Correspondence: gsengel@uchicago.edu

Cheng Wang and Moira L. Flanagan contributed equally to this work.

Editor: Julie Biteen.

http://dx.doi.org/10.1016/j.bpj.2016.10.017

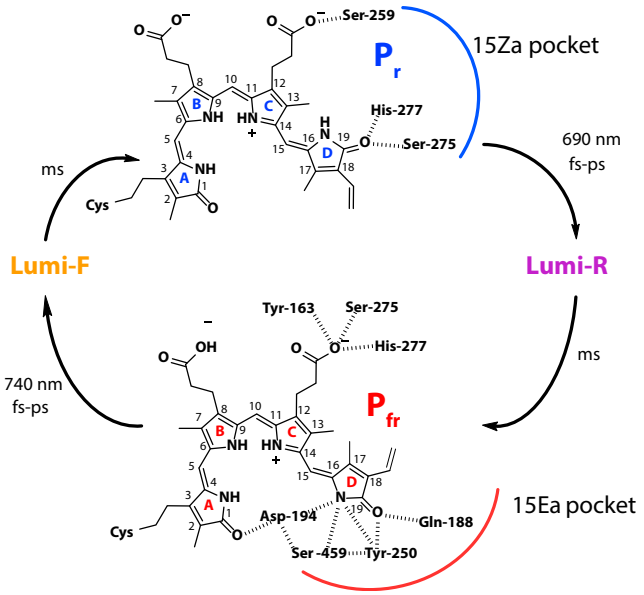

FIGURE 1 The interconversion of biliverdin-IXα between the P_r (15Za) and P_{fr} (15Ea) states. Amino acid labels are based on residue numbering of Pa. To see this figure in color, go online.

two-dimensional electronic spectroscopy (2D-ES) and comparing our data to these two models. The timescale of the initial double bond isomerization was recently associated with a 30 ps component in a cyanobacteriophytochrome (Cph1Δ2) (20), significantly longer than that of isomerizations in rhodopsin, bacteriorhodopsin, and photoactive yellow protein (0.2–3 ps) (21–23). Detailed analysis of the multiexponential decays is required to understand such slower dynamics. The multiexponential decays are sometimes interpreted as a collection of separate populations relaxing through parallel pathways of intermediates (15,19), but other studies have proposed a homogeneous explanation in which a single population relaxes through sequential intermediates (11,16). It is experimentally difficult to determine the origin of multiexponential behavior because heterogeneous populations cannot be resolved by conventional spectroscopies. Hence, prior work has varied in the explanation for these dynamics. For example in 2007, van Thor et al. (15) concluded that structural heterogeneity of the pigment-protein complex in Cph1 results in multiple populations relaxing through parallel pathways, but later revised the conclusion to include the possibility of the homogeneous model for the same protein in 2009 (18). Freer et al. (24) attributed spectroscopic differences to chemical heterogeneity, or chemically distinct chromophores in cyanobacteriophytochrome Tlr0924. However, the same research group later reported on dynamic heterogeneity in Cph1 that is dependent on the structure of the ground P_r state, which cannot be explained by chemical heterogeneity (19). Unlike many ultrafast spectroscopies employed in prior studies, 2D-ES resolves both the pump and probe axes and is therefore able to directly test whether heterogeneity of transition energies is correlated to heterogenous dynamics.

The source of separate populations in the heterogeneous explanation is not entirely clear. In a protein environment it is common to see an array of diverse conformations, each with a slightly different electrostatic environment of the cofactor, giving rise to a range of transition energies. The timescales of transformations between these conformations typically span femtoseconds to nanoseconds, but transition times between structurally very different conformations can take up to many seconds. In an ultrafast measurement, all of the processes that occur on a timescale longer than the duration of the experiment are effectively frozen and manifest as structural heterogeneity in the ensemble, associated with a range of populations and transition energies (25). Therefore, we expect heterogeneity in the ground state, and indeed, such structural heterogeneity in the ground state is supported by single molecule fluorescence spectroscopy (26), resonance Raman spectroscopy (27), fluorescence line narrowing spectroscopy (28), ^{13}C-^{1}H HETCOR NMR (29), and pump-probe studies at multiple pumping wavelengths (19). However, it remains unclear whether the spectroscopic variations due to structural heterogeneity result in qualitative differences in the subsequent photodynamic pathways (30,31).

2D-ES (32,33) can probe the photoinitiated dynamics on ultrafast timescales and display the dynamics in a series of time-resolved 2D correlation maps (34–37). A review of 2D-ES and its applications by Cho et al. (32) is both understandable and eloquent. 2D-ES has been applied to study spectral diffusion (34,38,39), photosynthetic light-harvesting complexes (40–46), semiconducting nanocrystals (47–50), and atomic vapors (51–54). Unlike traditional pump-probe experiments, 2D-ES correlates excitations at different energies with the fates of the excited states across the entire excitation window. Heterogeneity that is static on the timescale of the experiment is evident as populations that absorb slightly different wavelengths of light. Consequently, the inhomogeneously broadened spectroscopic feature in the 2D-ES map will appear elongated along the diagonal. Spectroscopic peaks can also be broadened by randomization due to the environment and ultrafast relaxation of the chromophore and its environment. If these motions are fast on the timescale of the experiment, the peak will appear round and symmetric. More typically, the motions that would broaden the feature are slow compared to our experimental pulse lengths (12 fs) but fast compared to our longest waiting times (400 ps). Under these conditions, we see elongated features at short waiting times (e.g., $T = 0$ fs to $T = 100$ fs), but the features expand uniformly in both coordinates and appear as a round peak in 2D-ES data at longer waiting times ($T = 400$ ps). That is, 2D-ES separates broadening in the homogenous and inhomogeneous limits along distinct spectral axes and allows observation of the dynamics on the appropriate timescales between these two limits. The dynamics of subpopulations with transitions of different energies can thus be tracked separately. For clarity, we use the terms

"homogeneous broadening" and "inhomogeneous broadening" as they are used in ultrafast spectroscopy to describe spectroscopic features, but reserve "heterogeneity" and "homogeneity" to describe variations (or lack thereof) in conformations and transition energies. For example, a peak is initially inhomogeneously broadened in 2D-ES because of heterogeneity in the sample, but at longer times may appear homogeneously broadened as the system loses memory of its initial conformation.

In this work, we examine the dynamics of the photosensory core modules containing the PAS-GAF-PHY domains of two bacteriophytochromes with distinct ground states and photodynamics: RpBphP2 (P2) from *R. palustris* and PaBphP (Pa) from *Pseudomonas aeruginosa* (6,55,56). Unlike the canonical bacteriophytochrome P2, Pa adopts the P_{fr} ground state in the dark and efficiently transforms to the P_r state upon activation with far-red light. The quite different photoconversions in these two core modules enables us to examine both $P_r \rightarrow$ Lumi-R and $P_{fr} \rightarrow$ Lumi-F transformations.

MATERIALS AND METHODS

Spectroscopy

The experimental apparatus is shown in Fig. S1 in the Supporting Material. A 5 kHz, 600 μJ pulse train centered at 800 nm from a Legend Elite regenerative amplifier (Coherent, Santa Clara, CA) was focused into a 2 m tube containing 1.5 atm of argon gas to generate ultra-broadband pulses spanning from 450 to 900 nm. The white light pulses were compressed by negatively chirped mirrors and a pulse shaper. The pulse duration was measured at the sample position to be ~12 fs by transient grating frequency resolved optical gating (*TG-FROG*; Fig. S2). The beam was then directed into the 2D-ES apparatus described in Zheng et al. (57). To avoid multiexciton effects, an attenuated pulse energy of 15 nJ/pulse was used in the experiment. Rephasing 2DES data were collected over a range of coherence times from 0 to 90 fs in 1.5 fs increments and a range of waiting times (corresponding to the delay time in pump-probe spectroscopies) from −50 fs to 400 ps. Steps of 5 fs were used over the 0–700 fs range and logarithmically thereafter. We used separately collected transient absorption spectra to phase each 2D spectrum (37,58). The transient absorption spectra were collected with the same laser pulse as that in the 2D-ES experiment and the beam was attenuated to achieve a pump pulse of 50 nJ/pulse and probe pulse power of 0.4 nJ/pulse.

Sample preparation

The photosensory core modules of the RpBphP2 and PaBphP bacteriophytochromes were coexpressed in *Escherichia coli* BL21 with heme oxygenase as described in Yang et al. (4). The protein was purified on a Ni-NTA affinity column. The column was washed with 20 mM Tris buffer (pH 8) and 1 M NaCl, then with sonication buffer. Protein was eluted with 20 mM Tris buffer (pH 8), 50 mM NaCl, and 300 mM imidazole, and purity was monitored by absorption spectrum. The protein was then washed and concentrated on Amicon UltraCentrifugal Filters (Millipore, Billerica, MA).

The protein solution was contained in a quartz flow cuvette with 200 μm path length. A peristaltic metering pump was used to flow fresh sample to the cuvette from an external reservoir with 3 mL sample volume. LED light of 690 or 740 nm was used to illuminate the external reservoir. The LED light total power was 20 mW for experiments on both Pa and P2. The samples had an absorbance at 700 nm of 0.2–0.3 O.D. in a path length of 200 μm.

RESULTS AND DISCUSSION

$P_r \rightarrow$ Lumi-R conversion of P2

As shown in Fig. 2, P2 adopts the P_r state in the dark, with an absorption peak at 709 nm and a vibronic shoulder at 647 nm. With continuous illumination at 690 nm, P2 partially converts to P_{fr} state, evident in the linear spectrum as a shoulder at 754 nm. Similar partial conversion with light activation at similar wavelengths is reported in Yang et al. (4). Partial conversion may arise from significant spectral overlap between P_{fr} and P_r states, leading to significant $P_{fr} \rightarrow P_r$ back conversion under the LED light.

2D-ES data were acquired for P2 in the dark ($P_r \rightarrow$ Lumi-R conversion) for a series of waiting times. The end result is a series of 2D energy correlation maps each associated with a different waiting time. As shown in Figs. 3, *a* and *b*, and S3, positive signals on the 2D maps are associated with stimulated emission/ground state bleach, while negative signals are associated with excited state absorption or induced absorption. Together, these data illustrate how excited states evolve in time and reveal both relaxation and interconversion between different subensembles within the states (25).

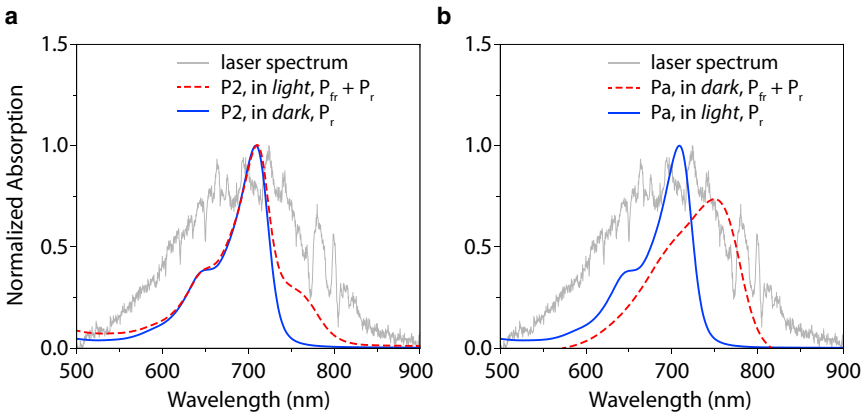

FIGURE 2 Absorption spectra of the P2 and Pa overlaid with the laser spectrum (*gray*). (*a*) P2 in dark, in the P_r state; P2 with illumination of 690 nm LED light, in a mixture of P_r and P_{fr} states; laser spectrum. (*b*) Pa with illumination of 740 nm LED light, adopting the P_r state; Pa in dark, in a mixture of P_r and P_{fr} states; laser spectrum. To see this figure in color, go online.

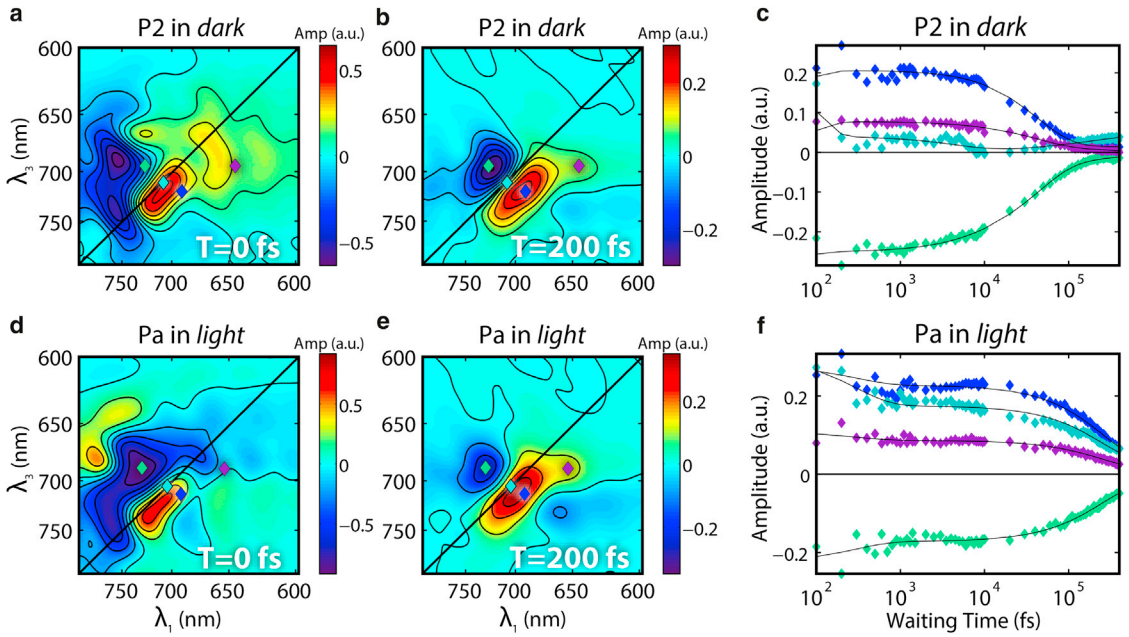

FIGURE 3 2D-ES of the P2 in the P_r state: (*a*) at $T = 0$ fs; (*b*) at $T = 200$ fs. 2D-ES of the Pa in the P_r state: (*d*) $T = 0$ fs; (*e*) $T = 200$ fs. Time traces of representative points marked by colored diamonds on the 2D-ES: (*c*) P2 in the P_r state and (*f*) Pa in the P_r state. The time trace data and their corresponding positions on the 2D maps are marked with the same color. Lines are fittings of the data according to Eq. 1. To see this figure in color, go online.

In rephasing 2D-ES data, homogeneous broadening widens the spectral line in both frequency axes on the 2D-ES map as time progresses. That is, the peak becomes rounder with time because there is less correlation with the initial state as the experiment progresses. In contrast, inhomogeneous broadening elongates the peak only along the diagonal because the photon echo eliminates inhomogeneous broadening in the antidiagonal direction. In the case of P2, the BV chromophore is embedded in an apo-protein environment. Although protein fluctuations homogeneously broaden the peak in the 2D-ES data, the solvation response to the BV excitation can be thought of as practically static because the timescale of our experiments is much faster than many protein rearrangements (25). Ground state heterogeneity manifests in the 2D-ES maps as a peak elongated along the diagonal, indicating a distribution of BV with slightly different initial transition energies that do not significantly change on the femtosecond-to-400-picosecond timescale. The 2D-ES spectrum of P2 in the P_r state shows clear elongation along the diagonal at $T = 0$ fs (Fig. 3 *a*), consistent with ground state heterogeneity. This elongation persists at longer waiting times (Figs. 3 *b* and S4). Therefore, we conclude that there is indeed ground state heterogeneity present in agreement with the literature (15,19,27,29).

The intensities of the signal on the main diagonal showed oscillatory beating in waiting time with a periodicity of ~26 fs. This beating is consistent with a vibrational mode of 1253 cm^{-1}, which can be assigned to C-H rocking of the vinyl groups or the N-H rock/C-C stretch mode in BV (30) (Fig. 4). Our frequency resolution of these beating signals is limited to ~50 cm^{-1}, preventing more precise assignment of the observed vibrations. The distribution of

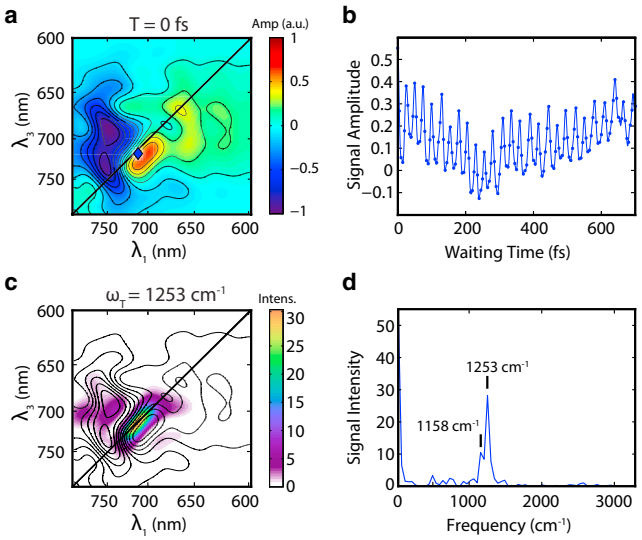

FIGURE 4 Beating signals of P2 in the $P_r \rightarrow$ Lumi-R process. (*a*) 2D-ES map at $T = 0$ fs with contours. (*b*) Fourier interpolated time trace taken at $\lambda_1 = 712$ nm and $\lambda_3 = 718$ nm marked by the blue diamond on the 2D plot in (*a*). The trace shows a beating signal with periodicity at ~25 fs. (*c*) Distribution map of the beating power at 1253 cm^{-1}. The heat map encodes the strength of the power spectrum at 1253 cm^{-1}. Contours of the 2D-ES at $T = 0$ fs are overlaid on the figure. (*d*) Fourier transform of the time trace in (*b*), showing peaks at 1253 cm^{-1} and 1158 cm^{-1}, possibly associated with the vinyl C-H rocking vibrational modes. To see this figure in color, go online.

power intensity of the beating at 1253 cm^{-1} is shown in Fig. 4. The distribution exhibits an elongated diagonal peak (Fig. 4 *c*), consistent with vibrational motion on the ground state surface. The beating extends well beyond a 1 ps waiting time. A second beating frequency of 1158 cm^{-1} was also present, which occupies a region slightly above the diagonal in the 2D map (Fig. S5 *c*). The initial phase of this 1158 cm^{-1} mode shows a 90° shift from the 1253 cm^{-1} mode (Fig S5, *e* and *f*), and we attribute this beating signal to a vibrational motion on the excited state surface. Definitive assignment of this excited state mode is difficult. We are inclined to attribute this motion on the excited state surface to the same mode we see on the ground state because the wavepacket motion during the coherence time evolves in that direction. However, this excited state vibration may also be associated with the C-H vinyl rocking or the N-H rock/C-C stretch. Additional modes associated with the C=C stretch and hydrogen out-of-plane motions are also present and displayed in Fig. S6.

The intensities of the spectra at longer waiting time (70 fs to 400 ps) and larger time intervals (semilog spacing) were fitted to a sum of three exponential decays (Fig. 3, *a–c*). A global fitting was first carried out to give three global lifetimes and maps of three preexponential factors (A_1–A_3) together with a residual constant term A_4 as shown in Eq. 1:

$$y = A_1(\lambda_1,\lambda_3)e^{-\frac{t}{\tau_1}} + A_2(\lambda_1,\lambda_3)e^{-\frac{t}{\tau_2}} + A_3(\lambda_1,\lambda_3)e^{-\frac{t}{\tau_3}} + A_4(\lambda_1,\lambda_3). \quad (1)$$

The values of A_1–A_4 are dependent on both the excitation and emission wavelengths, and can be plotted as 2D maps. We refer to them as the decay-associated spectra (DAS, Figs. 5, *a–d*, and S7 *a*), analogous to decay-associated difference spectra in pump-probe spectroscopy. The constant residue term A_4, is approximately equivalent to the 2D-ES at long waiting time, and represents the portion of the spectrum that remains after the decay of components A_1–A_3. Therefore, we associate it with the spectrum of the Lumi-R state (Fig. S7). The spectrum of Lumi-R mainly contains a positive ground-state bleach signal overlaid with weak negative excited state absorption from its photogeneration. The lifetimes associated with A_1–A_3 from this global fitting are $\tau_1 = 0.045$ ps, $\tau_2 = 4.8$ ps, and $\tau_3 = 42$ ps. The values of τ_2 and τ_3 are very similar to those reported by Toh et al. (5) from pump-probe spectroscopy for a similar bacteriophytochrome RpBphP3 ($\tau_1 = 0.4$ ps, $\tau_2 = 4$ ps, $\tau_3 = 43$ ps, and $\tau_4 = 170$ ps). We attribute our lower value of τ_1 to our shorter pulse width, enabling us to detect early dynamics more accurately. Toh et al. (5) also identify a 170 ps component by both pump-probe and time-resolved fluorescence measurements. This component connects the excited state and ground state surfaces, and they attribute it to heterogeneity of the sample. However, we did not observe such a component. If we add a fourth exponential component with lifetime constrained to be >100 ps in the fitting algorithm, we obtain $\tau_4 = 226$ ps but its amplitude is negligible compared to those of the other three exponential components.

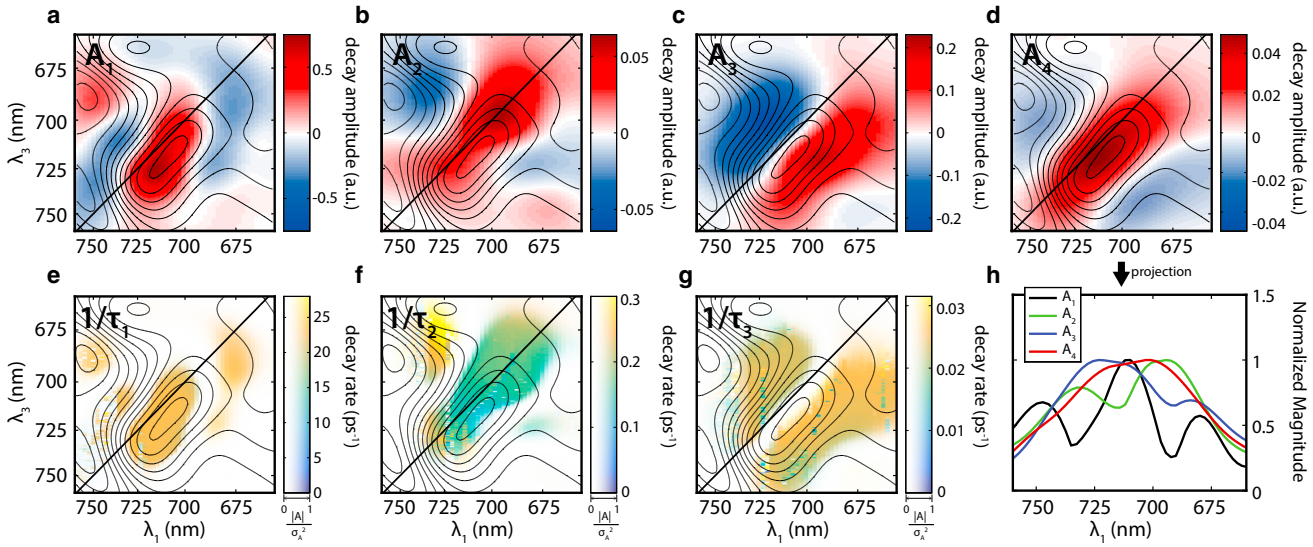

FIGURE 5 DAS support a homogeneous dynamic model for the P2 $P_r \rightarrow$ Lumi-R conversion. (*a–d*) A_1–A_4 terms of DAS of P2 in the P_r state from global fitting to Eq. 1. The 2D-ES map at $T = 0$ fs is also overlaid for reference (contours in all panels). (*e–g*) Variations of the exponential decay rates $1/\tau_1$, $1/\tau_2$, and $1/\tau_3$ in ps^{-1}. Different rates are encoded by the heat map gradiations, and the drawing is also gated by DAS magnitude with a transparency map, so that the regions with smaller DAS magnitudes will show lighter on the figure, as shown by transparency axis on the color bar. The transparency map is determined by the normalized magnitude of the DAS component divided by the variance of its fit. (*h*) Projection of the absolute value of the DAS to the λ_1 axis (absorption or pump axis) to represent the excitation range of the observed signal. All four DAS components cover the same range of pump wavelengths. The dips in the projections arise from cancellation between positive and negative signals. To see this figure in color, go online.

The existence of multiple lifetimes in the photodynamics of P2 can be explained by either a heterogeneous model with functionally distinct pathways or a homogeneous model involving sequential intermediates. In the heterogeneous model, components with different lifetimes are associated with different ground state subpopulations of the protein. That is, separate populations undergo distinct decay pathways. In contrast, the homogeneous model assigns the multiple DAS components to a sequence of intermediates of a single chemical moiety. With our 2D-ES DAS maps on hand, we can test these two models. If ground state heterogeneity exists, we expect inhomogeneous broadened peaks located across different pump wavelengths for each DAS component. In contrast, in the homogeneous model of sequential intermediates, the DAS components should occupy roughly the same region of the pump wavelengths. We have projected the absolute values of the DAS to their λ_1 axes to represent the pumping range of each DAS. As shown in Fig. 5 *h*, all the four DAS components possess a very similar pumping wavelength, consistent with a homogeneous model of sequential intermediates. The dips in the projections arise from the cancellation between positive and negative signals.

To further investigate possible heterogeneity within each DAS component, we allowed the lifetimes and amplitudes from the global fitting to be refined independently for each pixel on the 2D-ES map. This enables us to explore whether the fitted lifetimes vary across an inhomogeneously broadened peak. If so, this would indicate heterogeneity in the photodynamics. Such an individual refinement using the values of global fitting as starting points can be represented by Eq. 2:

$$y = A_1'(\lambda_1,\lambda_3)e^{-\frac{t}{\tau_1'(\lambda_1,\lambda_3)}} + A_2'(\lambda_1,\lambda_3)e^{-\frac{t}{\tau_2'(\lambda_1,\lambda_3)}} + A_3'(\lambda_1,\lambda_3)e^{-\frac{t}{\tau_3'(\lambda_1,\lambda_3)}} + A_4'(\lambda_1,\lambda_3). \quad (2)$$

As shown in Fig. S8, the amplitude maps (DAS) for the individual fittings are very similar to that of the global fitting. When these maps are compared by subtraction, negligible residuals are obtained as shown in Fig. S9, confirming the robustness of the fitting algorithm. The fitting approach of Eq. 2 allows us to examine the distribution of lifetimes across the map. As shown in Fig. 5, *e–g*, the lifetimes from the individual fittings are plotted together with the contour line of the 2D-ES at $T = 0$ fs. The lifetimes are expressed in decay rates ($1/\tau$) in ps^{-1} and encoded by color. The rates are also gated by the corresponding DAS amplitudes through an intensity (transparency) coding. For example, lifetimes in regions of negligible DAS intensities are shown in white. The $1/\tau_1$ and $1/\tau_3$ rates are found to distribute evenly across inhomogeneously broadened features on the 2D maps in Fig. 5. The $1/\tau_2$ component exhibits a rate that is 1.5 times faster in regions of excited absorption, indicating that the process of vibrational relaxation has a slightly different rate on the excited state surface. Nevertheless the variation of the rate constants across the map is small, and supports a homogeneous dynamic model involving sequential intermediates. Finally, when we perform singular value decomposition (SVD) on the data cube, two components are found, one dominant component with multiple exponential decays and one weak component with contributions only ~5% of the total amplitude and a lifetime of 0.1 ps.

These analyses by different routes all suggest that the system can be best modeled by a single population with homogeneous multiexponential dynamics.

All possible models with three different decay components have been examined, and the species-associated spectra corresponding to each model were constructed. Three possible models are identified. We prefer the model shown in Fig. 6, for its simplicity and adequacy in explaining all experimental observations. The other two candidate models are presented in Figs. S10 and S11, and we note that our data is consistent with all three models.

In our proposed model, after excitation to the Franck-Condon region ($^{FC}P_r^*$), two stages of vibrational relaxation involving two independent nuclear coordinates lead to $^{rel}P_r^*$ with time constants of τ_1 and τ_2. This state then proceeds over a transition barrier resulting from

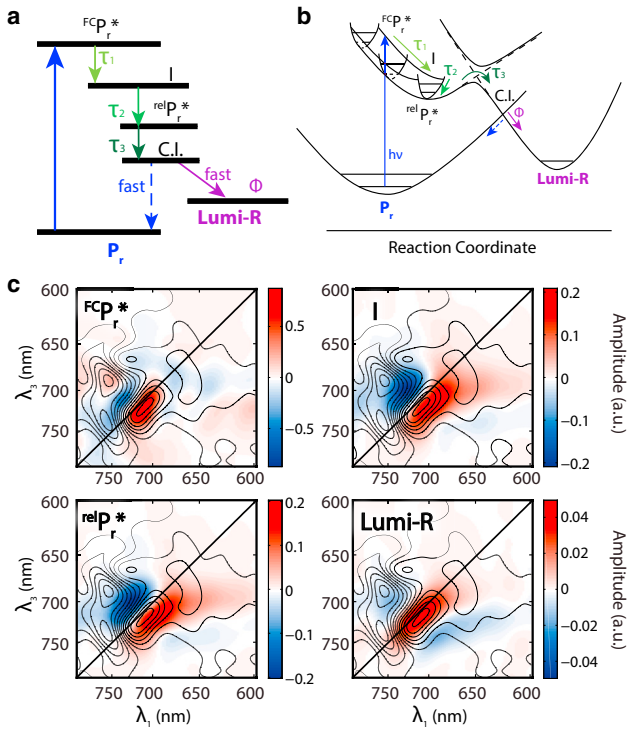

FIGURE 6 Proposed model of the P_r to Lumi-R conversion in P2. (*a*) The model to describe dynamics of the P2 in the $P_r \rightarrow$ Lumi-R transformation. (*b*) Proposed reaction surface geometry. (*c*) Species-associated spectra of the corresponding species. To see this figure in color, go online.

avoided crossing between the P_r* excited state surface and the Lumi-R ground state surface, with typical time τ_3, and then proceeds to the Lumi-R product on the ground state surface. Before reaching the bottom of the Lumi-R state, a conical intersection (CI) between the Lumi-R ground state surface and the P_r ground state surface is encountered. The system either proceeds to the Lumi-R with a quantum efficiency of Φ or reverts to P_r at the CI.

$P_r \rightarrow$ Lumi-R conversion of Pa

As shown in Fig. 2 *b*, Pa in dark adopts the P_{fr} form, with an absorption peak at 750 nm and a vibrational shoulder at 686 nm. Upon continuous illumination of an LED light at 740 nm, the Pa converts completely to the P_r state with an absorption peak at 700 nm (Fig. 2 *b*). We first examined the $P_r \rightarrow$ Lumi-R conversion of Pa.

2D-ES was taken for Pa with continuous illumination of the LED light of 740 nm to populate its P_r state. As shown in Fig. 3, *d* and *e*, similar to P2 in the 2D-ES, Pa in its P_r state gives an inhomogeneous broadened peak. The signals were also beating in waiting time, consistent with a vibrational mode of 1064 cm^{-1} (Fig. S12). A map of the beating intensity at 1064 cm^{-1} exhibited an elongated diagonal peak (Fig. S12 *c*) and a separate peak in the excited state absorption region, indicating a similar vibrational frequency on the ground state and excited state surfaces. The time evolution dynamics of the spectra, however, is distinct from that of P2, as shown in Fig. 3. Similar global fitting was applied to obtain two time constants $\tau_1 = 0.31$ ps and $\tau_2 = 251$ ps. The preexponential amplitude maps (DAS) were again refined with the lifetime at individual spots on the 2D maps. The projected absolute values of the DAS on the λ_1 axis again overlap with each other, supporting a homogeneous model involving sequential intermediates (Fig. S13). Consistent with this hypothesis, SVD analysis also gives only one major component of the dynamic data. The shorter component $1/\tau_1$ shows different rates in different locations on the 2D-ES map, indicating different rates of vibrational relaxation on the ground state and excited state surfaces. The long component $1/\tau_2$, corresponding to the isomerization, is distributed much more evenly on the 2D-map, consistent with the homogeneous dynamic model involving sequential intermediates (Fig. S14). The τ_2 component of Pa is much slower than the corresponding component of P2, indicating a higher barrier before the conical intersection.

After an experimental analysis identical to that previously applied to P2, we propose a model very similar to that of P2 (Fig. S15). The major difference between the $P_r \rightarrow$ Lumi-R kinetic models of the P2 and the Pa is the substantially different barrier height before the CI, leading to very different rates of conversion.

$P_{fr} \rightarrow$ Lumi-F conversion of P2

Under illumination at 690 nm, we can partially convert the P2 protein to the P_{fr} state (Fig. 2 *a*). Because the conversion is not complete, the illuminated sample is a mixture of the P_r and the P_{fr} states. When we performed 2D-ES on this sample, SVD analysis showed two major components for the dataset, consistent with a mixture of P_r and P_{fr} states. The 2D spectrum of the mixture clearly showed additional peaks at 740 nm, arising from the excitation wavelength of P_{fr}, distinct from that of the pure P_r state (Fig. S16). This is also shown on the projected DAS on the λ_1 axis (Fig. S19). Direct global fitting 2D-ES dynamics of the mixture gives four lifetimes: $\tau_1 = 0.27$ ps, $\tau_2 = 5.8$ ps, $\tau_3 = 39$ ps, and $\tau_4 = 151$ ps (Figs. S16–S19). We tried to separate the P_{fr} component by subtracting a certain percentage of the P_r 2D-ES from the mixture spectrum, in which the percentage of the P_r form was refined as an independent parameter, and estimated to be 49%. The isolated P_{fr} component was fitted to three exponentials with $\tau_1 = 0.97$ ps, $\tau_2 = 2.0$ ps, and $\tau_3 = 50.5$ ps. Because this spectrum separation algorithm is of limited effectiveness due to numerous fitting parameters and significant spectral overlap between the P_{fr} and the P_r states, we did not pursue analysis in this direction any further.

The 2D beating spectrum is very different from that in the $P_r \rightarrow$ Lumi-R conversion process (Figs. 7 and S20). A strong off-diagonal peak with excitation wavelength

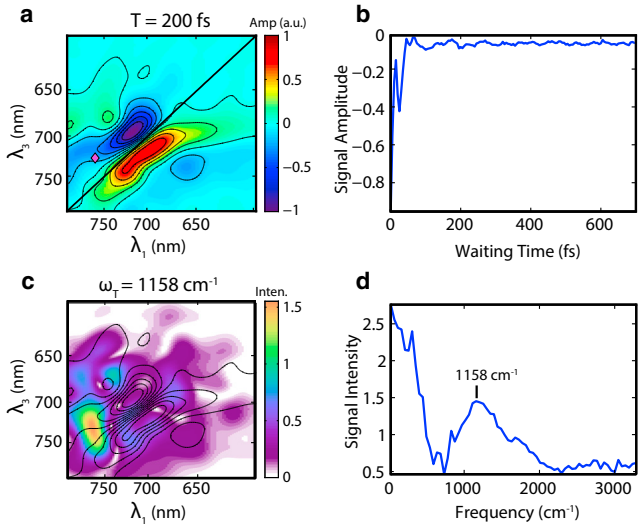

FIGURE 7 Beating signals of P2 in the mixed $P_{fr} \rightarrow$ Lumi-F and $P_r \rightarrow$ Lumi-R processes. (*a*) 2D-ES map at $T = 200$ fs with contours. (*b*) Time trace taken at $\lambda_1 = 764$ nm and $\lambda_3 = 726$ nm marked by the magenta diamond in (*a*). The trace shows a beating signal with periodicity at ~25 fs. (*c*) Distribution map of the beating power. The heat map encodes power spectrum intensity at 1158 cm^{-1}. Contours of the 2D-ES at $T = 0$ fs are overlaid on the figure. (*d*) Fourier transform of the time trace in (*b*), showing a broad peak centered at 1158 cm^{-1}, possibly associated with the vinyl C-H rocking vibrational modes. To see this figure in color, go online.

at >750 nm can be identified. This feature is associated with a broad peak in the ω_T domain centered at 1158 cm^{-1} with a FWHM of ~500 cm^{-1}, corresponding to a fast process of ~70 fs in the T domain. In agreement with this, the oscillating time trace in the T domain decays within 100 fs (Fig. 7 *b*).

P_{fr} → Lumi-F conversion of Pa

The solution of the Pa protein in the dark at room temperature probably contains a fraction of the P_r state, as indicated by its broad absorption spectrum (Fig. 2 *b*). Indeed, a related mutant Q188L even showed mixed P_r/P_{fr} states in the crystal structure (6,55). The SVD analysis of its 2D-ES also showed two major components. Direct global fitting of the 2D-ES dynamics gives three lifetimes: $\tau_1 = 0.18$ ps, $\tau_2 = 3.0$ ps, and $\tau_3 = 244$ ps. The third component $\tau_3 = 244$ ps is very similar to the τ_2 component from the P_r → Lumi-R conversion fitting (Figs. S21 and S22). We analyzed the spectrum after Fourier transforming in the T domain (Fig. S23), which showed similar off-diagonal features to those in the P2 P_{fr} → Lumi-F conversion at an excitation wavelength of >750 nm with a broad peak in the ω_T domain, indicating the fast dynamics.

CONCLUSIONS

The two bacteriophytochromes in this study show many similar characteristics, but their differences have the potential to elucidate the underlying principles. P2 and Pa both convert between P_r and P_{fr}, but adopt different conformations (P_r and P_{fr}, respectively) in their dark states. P2 and Pa also demonstrate quite different relaxation rates in their various interconversions. Notably, the two bacteriophytochromes possess different local hydrogen bonding between ring D of the BV and the surrounding polar residues in the protein pockets, which may account for the differences in rates (55). Two sets of residues around BV are important—the 15Ea pocket and the 15Za pocket (Fig. 1). Ring D of BV in the P_{fr} form resides in the 15Ea pocket, forming hydrogen bonds with the Asp-194, Tyr-250, Ser-459, and Gln-188 residues (4,6,55,56). Such interactions stabilized Pa in the P_{fr} dark state. In comparison, P2 has a mixture of polar and nonpolar residues in the corresponding three positions (Tyr, Leu, and Phe). The ring D resides in the 15Za pocket in the P_r form, interacting with a conservative His-277 residue and additional polar residues Ser-259 and Ser-275 for Pa (4,5). This interaction and other subtle differences in the chromophore binding pocket may slow down the Pa dynamics of P_r → Lumi-R (42 ps for P2; 251 ps for Pa).

The P_{fr} → Lumi-F photodynamics are generally faster than those of the P_r → Lumi-R process. The Fourier transforms over the T domain help isolate the oscillation signal from the P_{fr} → Lumi-F process with an excitation wavelength >750 nm. The broad peak in the ω_T domain arises from the ultrafast decay (<100 fs) of this oscillation. Such fast decoherence may be related to a CI on the P_{fr} → Lumi-F pathway (9,12). A proposed scheme is shown in Fig. S24, in which the initial P_{fr} state is excited to the vibronic excited state manifold, followed by fast leaking through a CI between the P_{fr} excited state surface and the Lumi-F ground state surface.

The P_r → P_{fr} and P_{fr} → P_r interconversions in phytochromes are initiated by ultrafast photoinduced isomerization of the chromophore (5,6). Previous spectroscopic studies of the isomerization have observed multiexponential decays, and have attributed these dynamics to the existence of ground state heterogeneity across the ensemble (10–15,18). In this work, we leverage the 2D resolution in 2D-ES to address whether ground state heterogeneity is indeed the origin of the functionally distinct relaxation pathways, as previously suggested. In 2D-ES, ground state heterogeneity is directly evident as an elongation of signal along the diagonal. Indeed, with lineshape analysis and global fitting, we were able to confirm the existence of this heterogeneity in the data (Fig. 2). We could then ask whether complexes with different transition energies (e.g., on the blue side of the elongated peak versus the red side) follow the same dynamics. In this manner, we separately analyze subensembles such as the red and blue edges of ground state heterogeneity, and compare results. Across the entire inhomogeneously elongated peak, we see strikingly similar dynamics. That is, despite the presence of ground state heterogeneity, we observe the same multiexponential decays (Fig. 5). This observation supports a model in which the multiexponential terms describe evolution on the excited state surface through sequential intermediates rather than distinct subpopulations following different pathways. Regardless of the transition energy to the initial excited state, the ensemble is functionally homogeneous on the excited state.

Because we observe no difference in the dynamics arising from ground state heterogeneity, we propose a model with just one component of P_r → Lumi-R relaxation and isomerization of the BV cofactor that includes a transition barrier between the Franck-Condon region and the CI degeneracy. This barrier accounts for multiexponential dynamics as well as the relatively slow CI isomerization compared to rhodopsin or photoactive yellow protein. This model applies to both P2 and Pa, although the relaxation rate constants differ between the two proteins. We attribute the different rates of the dynamics between P2 and Pa to the number and strength of hydrogen bonds between the ring D of BV and the residues in the 15Za pocket of the proteins. We now have a clearer understanding of the relationship between the tetrapyrrole cofactor and its apo-protein as they influence ultrafast isomerization dynamics. Future work is needed to establish the generality of these findings across the broader phytochrome family of proteins.

SUPPORTING MATERIAL

Twenty-four figures are available at http://www.biophysj.org/biophysj/supplemental/S0006-3495(16)30932-8.

AUTHOR CONTRIBUTIONS

C.W., M.L.F., and G.S.E. designed the research; C.W., M.L.F., R.D.M., H.Z., and A.R.G. carried out sample preparation and performed spectroscopic experiments; samples were provided by X.Y. and K.M.; data analysis was performed by C.W.; and the article was written by C.W., M.L.F., X.Y., K.M., and G.S.E.

ACKNOWLEDGMENTS

The authors thank the Defense Advanced Research Projects Agency (DARPA) QuBE program No. N66001-10-1-4060, the Air Force Office of Scientific Research (AFSOR) grant No. FA9550-10-1-0028, and the U.S. Department of Defense (DoD) Vannevar Bush Fellow Program grant No. N00014-16-1-2513, and the Camille and Henry Dreyfus Foundation, the Searle Foundation, and National Institutes of Health (NIH) grant No. EY024363 (to K.M. and X.Y.), for supporting the work in this publication. M.L.F. was supported in part by the National Institute of Biomedical Imaging and Bioengineering of the NIH under Award No. T32-EB009412.

REFERENCES

1. Butler, W. L., K. H. Norris, …, S. B. Hendricks. 1959. Detection, assay, and preliminary purification of the pigment controlling photoresponsive development of plants. *Proc. Natl. Acad. Sci. USA.* 45:1703–1708.
2. Davis, M. S., A. Forman, and J. Fajer. 1979. Ligated chlorophyll cation radicals: their function in photosystem II of plant photosynthesis. *Proc. Natl. Acad. Sci. USA.* 76:4170–4174.
3. Hughes, J., T. Lamparter, …, T. Börner. 1997. A prokaryotic phytochrome. *Nature.* 386:663.
4. Yang, X., E. A. Stojković, …, K. Moffat. 2007. Crystal structure of the chromophore binding domain of an unusual bacteriophytochrome, RpBphP3, reveals residues that modulate photoconversion. *Proc. Natl. Acad. Sci. USA.* 104:12571–12576.
5. Toh, K. C., E. A. Stojković, …, J. T. M. Kennis. 2010. Proton-transfer and hydrogen-bond interactions determine fluorescence quantum yield and photochemical efficiency of bacteriophytochrome. *Proc. Natl. Acad. Sci. USA.* 107:9170–9175.
6. Yang, X., J. Kuk, and K. Moffat. 2009. Conformational differences between the Pfr and Pr states in *Pseudomonas aeruginosa* bacteriophytochrome. *Proc. Natl. Acad. Sci. USA.* 106:15639–15644.
7. Rockwell, N. C., Y. S. Su, and J. C. Lagarias. 2006. Phytochrome structure and signaling mechanisms. *Annu. Rev. Plant Biol.* 57:837–858.
8. Bongards, C., and W. Gärtner. 2010. The role of the chromophore in the biological photoreceptor phytochrome: an approach using chemically synthesized tetrapyrroles. *Acc. Chem. Res.* 43:485–495.
9. Bischoff, M., G. Hermann, …, D. Strehlow. 1998. Ultrashort processes of native phytochrome: femtosecond kinetics of the far-red-absorbing form Pfr. *J. Phys. Chem. A.* 102:4399–4404.
10. Fitzpatrick, A. E., C. N. Lincoln, …, J. J. van Thor. 2012. Pump-dump-probe and pump-repump-probe ultrafast spectroscopy resolves cross section of an early ground state intermediate and stimulated emission in the photoreactions of the Pr ground state of the cyanobacterial phytochrome Cph1. *J. Phys. Chem. B.* 116:1077–1088.
11. Heyne, K., J. Herbst, …, R. Diller. 2002. Ultrafast dynamics of phytochrome from the cyanobacterium *Synechocystis*, reconstituted with phycocyanobilin and phycoerythrobilin. *Biophys. J.* 82:1004–1016.
12. Kim, P. W., L. H. Freer, …, D. S. Larsen. 2012. Femtosecond photodynamics of the red/green cyanobacteriochrome NpR6012g4 from *Nostoc punctiforme*. 1. Forward dynamics. *Biochemistry.* 51:608–618.
13. Kim, P. W., L. H. Freer, …, D. S. Larsen. 2012. Second-chance forward isomerization dynamics of the red/green cyanobacteriochrome NpR6012g4 from *Nostoc punctiforme*. *J. Am. Chem. Soc.* 134:130–133.
14. Kim, P. W., N. C. Rockwell, …, D. S. Larsen. 2013. Unraveling the primary isomerization dynamics in cyanobacterial phytochrome Cph1 with multi-pulse manipulations. *J. Phys. Chem. Lett.* 4:2605–2609.
15. van Thor, J. J., K. L. Ronayne, and M. Towrie. 2007. Formation of the early photoproduct Lumi-R of cyanobacterial phytochrome Cph1 observed by ultrafast mid-infrared spectroscopy. *J. Am. Chem. Soc.* 129:126–132.
16. Dasgupta, J., R. R. Frontiera, …, R. A. Mathies. 2009. Ultrafast excited-state isomerization in phytochrome revealed by femtosecond stimulated Raman spectroscopy. *Proc. Natl. Acad. Sci. USA.* 106:1784–1789.
17. Toh, K. C., E. A. Stojković, …, J. T. M. Kennis. 2011. Fluorescence quantum yield and photochemistry of bacteriophytochrome constructs. *Phys. Chem. Chem. Phys.* 13:11985–11997.
18. van Wilderen, L. J. G. W., I. P. Clark, …, J. J. van Thor. 2009. Mid-infrared picosecond pump-dump-probe and pump-repump-probe experiments to resolve a ground-state intermediate in cyanobacterial phytochrome Cph1. *J. Phys. Chem. B.* 113:16354–16364.
19. Kim, P. W., N. C. Rockwell, …, D. S. Larsen. 2014. Dynamic inhomogeneity in the photodynamics of cyanobacterial phytochrome Cph1. *Biochemistry.* 53:2818–2826.
20. Yang, Y., M. Linke, …, K. Heyne. 2012. Real-time tracking of phytochrome's orientational changes during Pr photoisomerization. *J. Am. Chem. Soc.* 134:1408–1411.
21. Grintsevich, E. E., I. E. Adzerikho, …, D. I. Metelitza. 2001. Polydisulfides of substituted phenols as effective protectors of peroxidase against inactivation by ultrasonic cavitation. *Biokhimiia.* 66:740–746.
22. van Brederode, M. E., T. Gensch, …, S. E. Braslavsky. 1995. Photoinduced volume change and energy storage associated with the early transformations of the photoactive yellow protein from *Ectothiorhodospira halophila*. *Biophys. J.* 68:1101–1109.
23. Pande, K., C. D. M. Hutchison, …, M. Schmidt. 2016. Femtosecond structural dynamics drives the trans/cis isomerization in photoactive yellow protein. *Science.* 352:725–729.
24. Freer, L. H., P. W. Kim, …, D. S. Larsen. 2012. Chemical inhomogeneity in the ultrafast dynamics of the DXCF cyanobacteriochrome Tlr0924. *J. Phys. Chem. B.* 116:10571–10581.
25. Jordanides, X. J., M. J. Lang, …, G. R. Fleming. 1999. Solvation dynamics in protein environments studied by photon echo spectroscopy. *J. Phys. Chem. B.* 103:7995–8005.
26. Nieder, J. B., M. Brecht, and R. Bittl. 2009. Dynamic intracomplex heterogeneity of phytochrome. *J. Am. Chem. Soc.* 131:69–71.
27. von Stetten, D., M. Günther, …, P. Hildebrandt. 2008. Chromophore heterogeneity and photoconversion in phytochrome crystals and solution studied by resonance Raman spectroscopy. *Angew. Chem. Int. Ed. Engl.* 47:4753–4755.
28. Nieder, J. B., E. A. Stojković, …, J. T. M. Kennis. 2013. Pigment-protein interactions in phytochromes probed by fluorescence line narrowing spectroscopy. *J. Phys. Chem. B.* 117:14940–14950.
29. Song, C., G. Psakis, …, J. Matysik. 2011. Two ground state isoforms and a chromophore D-ring photoflip triggering extensive intramolecular changes in a canonical phytochrome. *Proc. Natl. Acad. Sci. USA.* 108:3842–3847.
30. Spillane, K. M., J. Dasgupta, …, R. A. Mathies. 2009. Homogeneity of phytochrome Cph1 vibronic absorption revealed by resonance Raman intensity analysis. *J. Am. Chem. Soc.* 131:13946–13948.
31. Spillane, K. M., J. Dasgupta, and R. A. Mathies. 2012. Conformational homogeneity and excited-state isomerization dynamics of the bilin

chromophore in phytochrome Cph1 from resonance Raman intensities. *Biophys. J.* 102:709–717.

32. Cho, M. H., T. Brixner, …, G. R. Fleming. 2006. Two dimensional electronic spectroscopy of molecular complexes. *J. Chin. Chem. Soc. Taip.* 53:15–24.
33. Brańczyk, A. M., D. B. Turner, and G. D. Scholes. 2013. Crossing disciplines—a view on two-dimensional optical spectroscopy. *Ann. Phys. (Berlin).* 526:31–49.
34. Hybl, J. D., A. A. Ferro, and D. M. Jonas. 2001. Two-dimensional Fourier transform electronic spectroscopy. *J. Chem. Phys.* 115:6606–6622.
35. Jonas, D. M. 2003. Two-dimensional femtosecond spectroscopy. *Annu. Rev. Phys. Chem.* 54:425–463.
36. Cowan, M. L., J. P. Ogilvie, and R. J. D. Miller. 2004. Two-dimensional spectroscopy using diffractive optics based phased-locked photon echoes. *Chem. Phys. Lett.* 386:184–189.
37. Brixner, T., T. Mancal, …, G. R. Fleming. 2004. Phase-stabilized two-dimensional electronic spectroscopy. *J. Chem. Phys.* 121:4221–4236.
38. Wells, K. L., Z. Zhang, …, H.-S. Tan. 2013. Measuring the spectral diffusion of chlorophyll *a* using two-dimensional electronic spectroscopy. *J. Phys. Chem. B.* 117:2294–2299.
39. Hybl, J. D., A. Yu, …, D. M. Jonas. 2002. Polar solvation dynamics in the femtosecond evolution of two-dimensional Fourier transform spectra. *J. Phys. Chem. A.* 106:7651–7654.
40. Brixner, T., J. Stenger, …, G. R. Fleming. 2005. Two-dimensional spectroscopy of electronic couplings in photosynthesis. *Nature.* 434:625–628.
41. Read, E. L., G. S. Engel, …, G. R. Fleming. 2007. Cross-peak-specific two-dimensional electronic spectroscopy. *Proc. Natl. Acad. Sci. USA.* 104:14203–14208.
42. Selig, U., C.-F. Schleussner, …, T. Brixner. 2010. Coherent two-dimensional ultraviolet spectroscopy in fully noncollinear geometry. *Opt. Lett.* 35:4178–4180.
43. Schlau-Cohen, G. S., A. Ishizaki, and G. R. Fleming. 2011. Two-dimensional electronic spectroscopy and photosynthesis: fundamentals and applications to photosynthetic light-harvesting. *Chem. Phys.* 386:1–22.
44. Ginsberg, N. S., J. A. Davis, …, G. R. Fleming. 2011. Solving structure in the CP29 light harvesting complex with polarization-phased 2D electronic spectroscopy. *Proc. Natl. Acad. Sci. USA.* 108:3848–3853.
45. Harel, E., and G. S. Engel. 2012. Quantum coherence spectroscopy reveals complex dynamics in bacterial light-harvesting complex 2 (LH2). *Proc. Natl. Acad. Sci. USA.* 109:706–711.
46. Ostroumov, E. E., R. M. Mulvaney, …, G. D. Scholes. 2013. Energy transfer pathways in light-harvesting complexes of purple bacteria as revealed by global kinetic analysis of two-dimensional transient spectra. *J. Phys. Chem. B.* 117:11349–11362.
47. Turner, D. B., Y. Hassan, and G. D. Scholes. 2012. Exciton superposition states in CdSe nanocrystals measured using broadband two-dimensional electronic spectroscopy. *Nano Lett.* 12:880–886.
48. Griffin, G. B., S. Ithurria, …, G. S. Engel. 2013. Two-dimensional electronic spectroscopy of CdSe nanoparticles at very low pulse power. *J. Chem. Phys.* 138:014705.
49. Wong, C. Y., and G. D. Scholes. 2011. Biexcitonic fine structure of CdSe nanocrystals probed by polarization-dependent two-dimensional photon echo spectroscopy. *J. Phys. Chem. A.* 115:3797–3806.
50. Moody, G., R. Singh, …, S. T. Cundiff. 2013. Influence of confinement on biexciton binding in semiconductor quantum dot ensembles measured with two-dimensional spectroscopy. *Phys. Rev. B.* 87:041304.
51. Tian, P., D. Keusters, …, W. S. Warren. 2003. Femtosecond phase-coherent two-dimensional spectroscopy. *Science.* 300:1553–1555.
52. Dai, X., A. D. Bristow, …, S. T. Cundiff. 2010. Two-dimensional Fourier-transform spectroscopy of potassium vapor. *Phys. Rev. A.* 82:052503.
53. Tekavec, P. F., G. A. Lott, and A. H. Marcus. 2007. Fluorescence-detected two-dimensional electronic coherence spectroscopy by acousto-optic phase modulation. *J. Chem. Phys.* 127:214307.
54. Li, H., A. D. Bristow, …, S. T. Cundiff. 2013. Unraveling quantum pathways using optical 3D Fourier-transform spectroscopy. *Nat. Commun.* 4:1390.
55. Yang, X., J. Kuk, and K. Moffat. 2008. Crystal structure of *Pseudomonas aeruginosa* bacteriophytochrome: photoconversion and signal transduction. *Proc. Natl. Acad. Sci. USA.* 105:14715–14720.
56. Yang, X., Z. Ren, …, K. Moffat. 2011. Temperature-scan cryocrystallography reveals reaction intermediates in bacteriophytochrome. *Nature.* 479:428–432.
57. Zheng, H., J. R. Caram, …, G. S. Engel. 2014. Dispersion-free continuum two-dimensional electronic spectrometer. *Appl. Opt.* 53:1909–1917.
58. Singh, V. P., A. F. Fidler, …, G. S. Engel. 2013. Independent phasing of rephasing and non-rephasing 2D electronic spectra. *J. Chem. Phys.* 139:084201.